ACS Photonics
Article
pubs.acs.org/journal/apchd5

Nanoscale 3D Chiral Plasmonic Helices with Circular Dichroism at Visible Frequencies

Marco Esposito,*,† Vittorianna Tasco,† Massimo Cuscunà,† Francesco Todisco,† Alessio Benedetti,‡ Iolena Tarantini,§ Milena De Giorgi,† Daniele Sanvitto,† and Adriana Passaseo†

†National Nanotechnology Laboratory (NNL), Istituto Nanoscienze, CNR, via Arnesano, I-73100 Lecce, Italy
‡Università di Roma La Sapienza, Dip. SBAI, via Scarpa 16, 00161 Roma, Italy
§Università del Salento Dip., Mat-Fis Ennio De Giorgi, I-73100 Lecce, Italy

Supporting Information

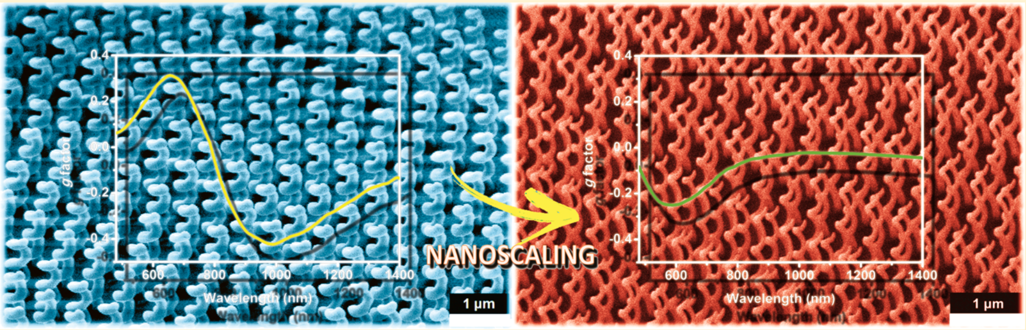

ABSTRACT: The nanoscaling of metamaterial structures represents a technological challenge toward their application in the optical frequency range. In this work we demonstrate tailored chiro-optical effects in plasmonic nanohelices, by a fabrication process providing a nanometer scale control on geometrical features, that leads to a fine tuning of operation band even in the visible range. Helicoidal 3D nanostructures have been prototyped by a bottom-up approach based on focused ion and electron beam induced deposition, investigating resolution limits, growth control and 3D proximity effects as a function of the interactions between writing beam and deposition environment. The fabricated arrays show chiro-optical properties at the optical frequencies and extremely high operation bandwidth tailoring dependent on the dimensional features of these 3D nanostructures: with the focused ion beam we obtained a broadband polarization selection of about 600 nm and maximum dissymmetry factor up to 40% in the near-infrared region, while with the reduced dimensions obtained by the focused electron beam a highly selective dichroic band shifted toward shorter wavelengths is obtained, with a maximum dissymmetry factor up to 26% in the visible range. A detailed finite difference time domain model highlighted the role of geometrical and compositional parameters on the optical response of fabricated nanohelices, in good agreement with experimental results.

KEYWORDS: *3D chirality, focused ion and electron beam induced deposition, nanophotonics, 3D proximity effect compensation, plasmonic metamaterial, circular dichroism*

In the last years, metamaterials have opened new paths in photonics applications, introducing properties and functionalities such as negative refractive index, cloaking and nanolasing.[1−3] Metamaterials are composed of engineered building blocks with subwavelength dimensions and exhibit properties of interaction with electromagnetic fields not found in nature.[4−6] Recently, renewed interest has focused on chiral metamaterials, where structural chirality results in a multitude of intriguing phenomena such as optical rotatory dispersion (ORD; i.e., rotation of the polarization state of light) and circular dichroism (CD; i.e., a different transmission level for a left and right circular polarized light).[7−14] Similar effects can be found in chiral molecules existing in nature (enantiomers). However, they exhibit small dipole moments performing a weak coupling to the interacting electromagnetic field and leading to extremely faint chiro-optical effects. To overcome such limitations, two-dimensional plasmonic chiral nanostructures, engineered to achieve a large electric dipole moment, have shown an efficient interaction with the incident light.[15,16] However, in order to maximize interaction with light, considering that the propagation of circularly polarized waves occurs through the torsion of the field vectors, the spatial arrangement of chiral metamaterials should present an evolution along the third dimension, that is, along the direction of light propagation, as occurred either in stacked unit cells realized by multistep electron beam lithography[17] (rosettes,[18] split-ring resonators[19]) or in quasi-three-dimensional objects.[20−23] The geometric structure closest to the ideal concept of chirality is the 3D

Received: August 28, 2014
Published: December 2, 2014

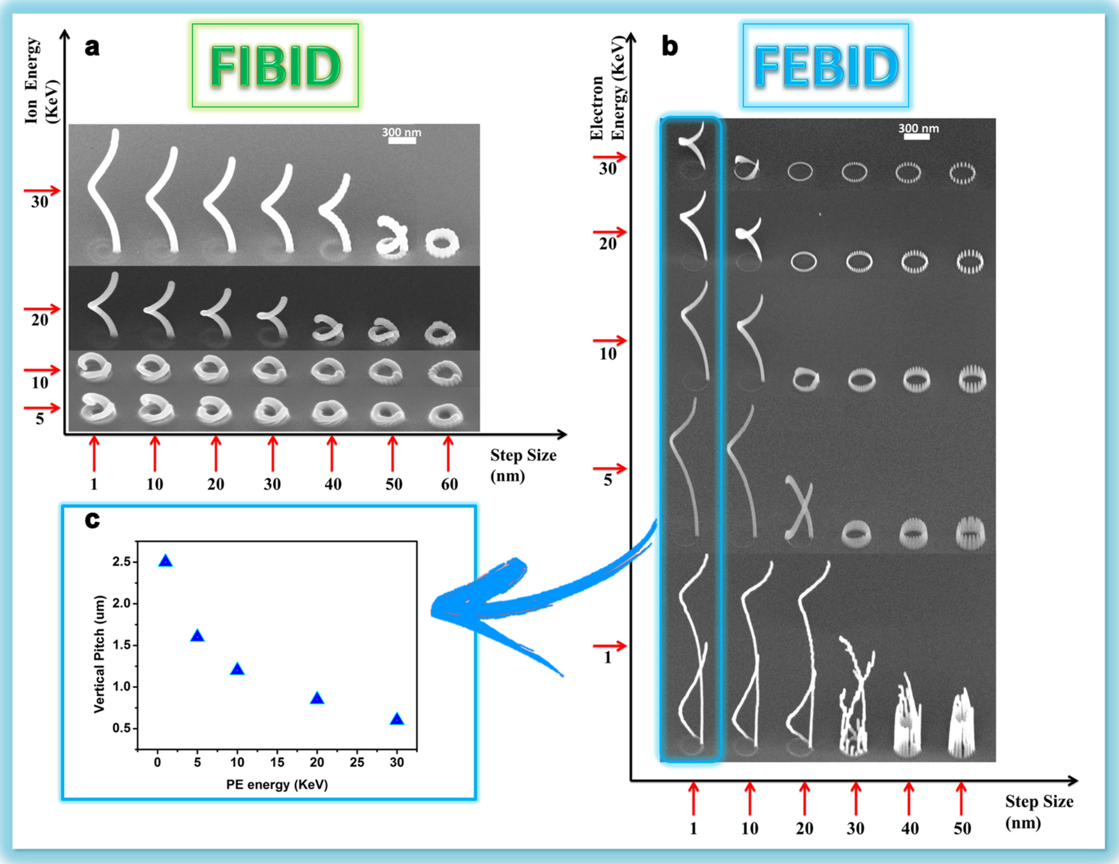

Figure 1. (a) SEM representation of the 3D FIBID nanohelix growth as a function of ion energy and step size. At low energies (<20 keV) the structures fail to detach from the surface for any value of the step size. Increasing the energy, nanohelices evolve along the *z* axis at different values of step size, allowing a wide flexibility of this fabrication approach toward design constraints at the nanoscale. The current value and the total dose were set, respectively, at 1 pA and 100 pC/μm. (b) 3D nanohelices realized by FEBID with constant dose (300 pC/μm), 10 μm aperture diameter but variable step size and electron energy. Contrary to FIBID process, at low energies the nanohelix VP increases, while at higher energies it decreases and the step size threshold gradually moves toward smaller values. (c) In FEBID process, the single loop nanohelix VP strongly depends on the primary electron acceleration voltage. This dependence is connected to the secondary electrons model[31,36−41] for the electron beam, where more secondary electrons are generated at low energies.

helix. Gansel et al. have realized 3D gold helices by Direct Laser Writing (DLW).[24,25] The characteristic sizes achieved in these chiral metamaterials limited their operation as circular polarizers to the IR range. Most recently, focused ion beam induced deposition (FIBID)[26,27] was successfully employed for the realization of nanohelices, showing a large circular dichroism factor in the near-infrared spectral region.[28] This approach allows realizing nanosystems of any shape and size by a single technological step with a highly precise spatial localization directly on the substrate and to control the three-dimensional evolution of planar structures. Further design flexibility can be accomplished switching from ion to electron beam induced deposition, thus shifting the operational photonic range toward shorter wavelengths.

In addition, focused electron beam induced deposition (FEBID) process,[27,29−31] being free of sputtering and ion implantation effects, is suitable for writing on structured substrates for optical applications (such as semiconductor heterostructures, photonic crystals) or on soft materials, such as polymers or biological samples, without inducing damages.[32]

However, the realization by FEBID and FIBID processes of complex 3D nanosystems, with spatial extension simultaneously in all the three space directions, requires a detailed investigation on many beam-precursor-substrate interactions resulting from 3D proximity effects that can be neglected in simpler structures such as dots and pillars, where the deposited volume grows primarily in one preferred direction.

In this work we show the effective nanoscaling of complex 3D nanosystems, consisting of single and arrayed platinum chiral nanohelices (CNH), by employing and comparing the FIBID and FEBID approaches. The physical and technological issues affecting this fabrication process were analyzed, emphasizing the importance of accurately understanding the physical role played by the experimental parameters in order to take full advantage of these powerful deposition techniques. Unwanted 3D proximity effects, which lead to structural deviation from the design, were controlled and limited, while keeping extremely high resolution at the nanometer scale. The 3D nanohelices fabricated by the FIBID and FEBID techniques demonstrated a strong chiral plasmonic activity, with size and compositional dependent circular dichroism at the visible and near-infrared frequencies. The effect of nanoscaling is strongly evidenced by the different optical behavior of the chiral structures. In particular, FIBID nanohelices show a broadband circular dichroism of about 600 nm, with a maximum dissymmetry factor value of ~40% at 1000 nm, while the improved resolution of FEBID approach leads to a highly selective dichroic band shifted toward shorter wavelength, reaching a maximum value of 26% at 600 nm.

A Finite Difference Time Domain (FDTD) model was developed to reproduce the transmittance spectra measured with left- and right-handed circularly polarized light, in relation to actual dimensions and composition of the investigated metamaterial, providing powerful guidelines for the customization and tailoring of a surface plasmon polariton helix-based metamaterials.

■ RESULTS AND DISCUSSION

3D Growth Dynamics and Structural Control for Pt Nanohelices by FIBID and FEBID Techniques. In order to fulfill design criteria for chiral metamaterials acting in a wide spectral range, with an operation band shifted to shorter wavelengths, a detailed comparison of the two approaches and related growth dynamic is of key relevance. In fact, FEBID, where the smaller size of the electron probe as compared to the ion beam probe provides nucleation sites of reduced area, can lead to a reduction of the achievable wire diameter (WD), which in turn allows shrinking both the external diameter (ED) and the vertical pitch (VP) of the helix due to a smaller filling factor (defined as the ratio between the platinum structure volume and the cylinder volume enclosing the nanostructure).

The first step toward the realization of 3D nanohelices was based on the achievement of highly controllable shape evolution by the two bottom-up techniques, FIBID and FEBID, respectively, employing an ion and an electron beam for metal deposition. So far, the investigation of the shape-dependent resolution limits and growth control in FIBID and FEBID applications was performed on structures with an unidirectional growth. Instead, the growth of more complex 3D nanostructures is heavily dependent on a complex system of beam—precursor—nanostructure interactions and on additional process parameters that govern the uniformity degree and spatial extension of the nanostructure in all directions by controlling the nucleation processes. Therefore, in this work, an extensive study on the dynamics of growth and on the beam and pattern parameters has been carried out for both techniques, in order to explore their resolution limits in relation to the key dimensional parameters of the 3D nanohelices (WD, ED, and VP). This study allowed us to develop a highly controlled fabrication method for manufacturing large array of 3D chiral nanostructures with strong optical activity in the visible range.

For the growth of a single 3D nanohelix we start from a planar empty circle scheme, with nanoscale features determined by the ion beam current and the accelerating voltage. In particular, the ion current monotonically affects the beam probe diameter and the number of particles, which are scattered during the writing process (sputtered atoms, ions and secondary electrons), determining the efficiency of the local precursor gas decomposition. The vertical evolution is then obtained by a proper balance of the beam and pattern parameters. In Figure 1a the 3D evolution as a function of ion energy and step size is illustrated. Here, the current value was kept constant (1 pA) for each value of accelerating voltage, whereas for each value of step size, the dwell time was adjusted in order to obtain a constant dose (100 pC/μm) at every beam energy. As is evident from Figure 1a, in this phase the role of ion energy is crucial. At low ion energy, the step size control does not allow the nanostructures to evolve into the third dimension, resulting in planar rings with increased wire radius. Only by increasing the ion energy, the basal ring starts to detach from the surface rising along the vertical axis, with a pitch value gradually increasing with energy. According to the model shown in refs 33−35, the increase in ion energy provides an increased amount of active material that leads to a higher vertical growth rate, improving also the localization of the deposited volume and, consequently, the resolution. Furthermore, at higher energies, the maximum step size allowing continuous structure evolution moves toward higher values (up to 40 nm for 30 keV energy), making the geometrical and technological parameters more flexible. Beyond these thresholds the overlap degree between successive spots becomes insufficient and leads to random generation of multibranches due to the structure breakage in several points.

In Figure 1b, the same analysis is reported for the 3D evolution of the single loop nanostructure, obtained by FEBID, as a function of the step size for increasing electron beam energies, fixing the dose at 300 pC/μm (by adjusting the dwell time accordingly). The beam aperture diameter was kept constant at 10 μm, with the electron current increasing with accelerating voltage. Contrary to the FIBID process, the nanohelix VP decreases with increasing primary electron (PE) energy (Figure 1c). As already known,[31,36−41] the vertical growth rate is directly dependent on the density of secondary electrons (SE) that is inversely proportional to the energy of the primary e-beam. In the examined electron energy range a coherent helix evolution is obtained only for very low step size values as a consequence of the probe diameter reduction with electron energy increase. At higher energies, the step size threshold that allows nanohelices to rush along the z-axis gradually moves toward smaller values (down to 1 nm for an energy of 30 keV). For a larger step size, each spot generates separated nucleation sites since the overlap between two consecutive spots is no more adequate to provide a continuous and uniform nucleation. However, at very low energy (1 keV), the density of the generated SE leads to the appearance of a secondary helix structure, when the step size values provide the necessary overlap. In this case, the added nucleation site is simply due to high density of secondary electrons generated by the transmitted e-beam through the primary growing helix.[42]

These preliminary considerations show that the controlled growth of complex 3D structures is the result of a complicated interplay between the density of supplied ions or electrons and the geometrical driving of decomposed material toward suitable and efficient nucleation sites along the 3D structure. While the density of nucleation sites is directly related to the step size, the dwell time finds a physical correspondence in the amount of deposited material in each deposition spot. A high level of control in the 3D growth of this kind of nanostructure can be obtained, first defining the highest nucleation site density (i.e., the minimum step size) providing a continuous z-axis structure evolution, and then providing the optimum deposit volume per spot (i.e., a sufficiently high dwell time) to obtain the desired vertical pitch, without further increasing the wire diameter (as described in the Supporting Information).

The understanding of growth dynamics of both FIBID and FEBID approach enabled us to accurately control the dimensional features of the proposed 3D nanostructures in a wide dimensional range, with a consequent shift of their spectral operating region: the WD can be varied from 130 down to 50 nm, whereas, at the same time, the VP can be scaled down to 200 nm.

Enhanced chiro-optical effects also require broadband operation which can be obtained by the coupling between a variable number of vertically stacked single loop helices.[43]

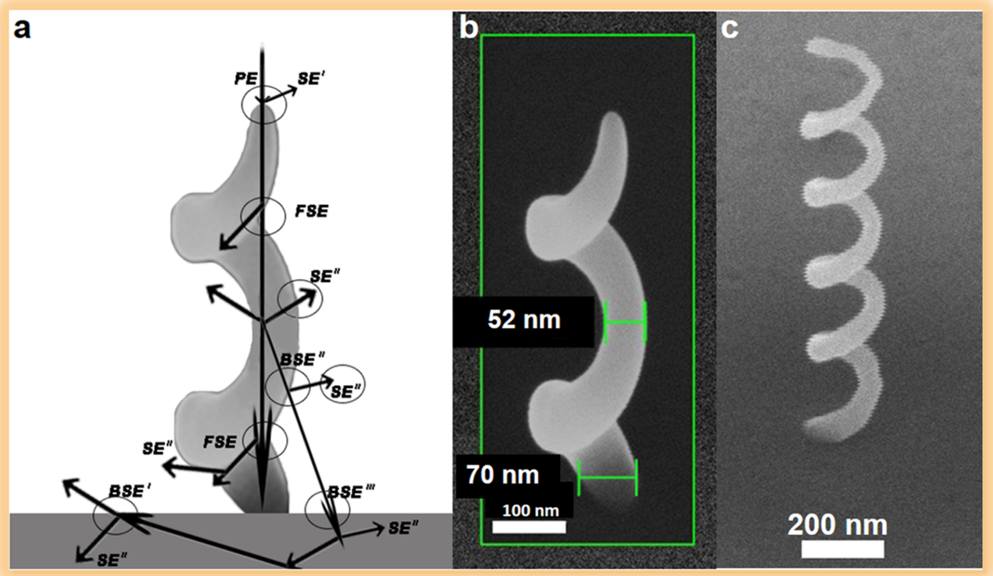

Figure 2. (a) Graphical representation of the different contributions to the shape evolution of multiscattered electrons. (b) SEM view of a two loop FEBID nanohelix. A WD negative gradient is shown along the vertical direction as the loop number increases. (c) Five-loop nanohelix realized by FEBID after dose compensation method[28] and 10 keV as accelerating voltage.

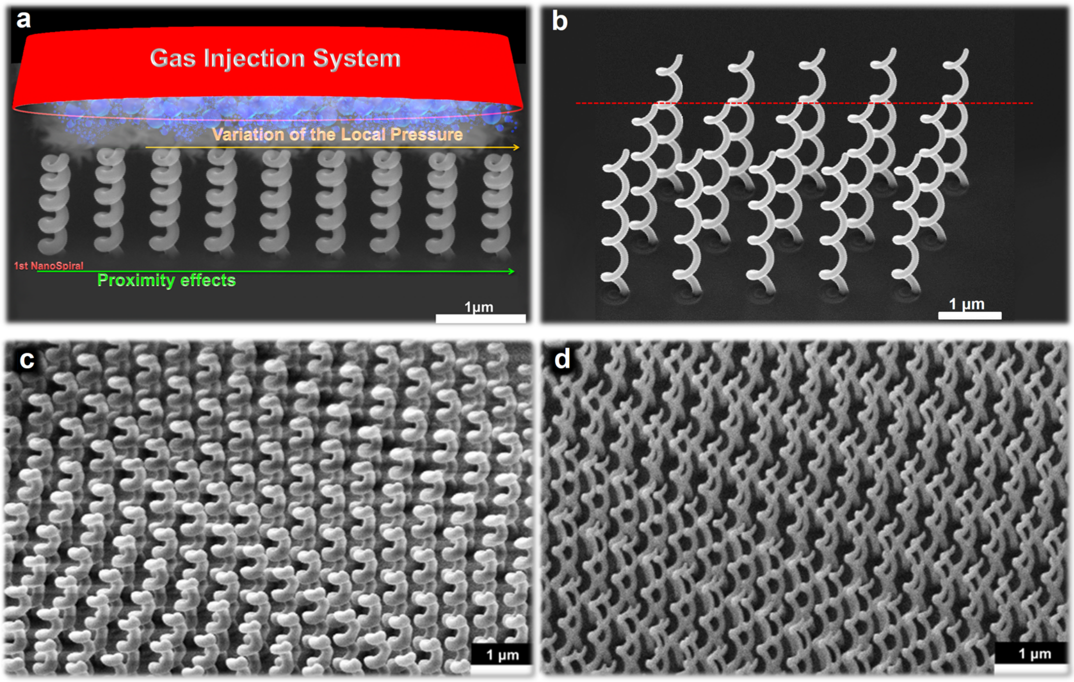

Figure 3. (a) Linear array of nanohelices along the x-axis. The growth process took place from left to right to avoid shadow effect. The gas supply is situated in front of the array. Precursor molecule reflection effect on each nanohelix, except for the first one, at constant local precursor pressure, entailing an extra molecule flow on the growing structure, due to the previous neighbor one, that increase the growth rate. The subsequent nanohelices exhibit a reduced height due to a slow pressure drop by effusion and a depletion of the molecular density in the writing area. (b) Nanohelices array with constant VP realized by inserting a refresh time of 2 min among the growth of individual nanostructures. (c) Array of 20 × 20 nanohelices (3 loops, ED = 400 nm, WD = 130 nm, VP = 300 nm, LP = 700 nm) fabricated by FIBID. (d) Array of 40 × 40 nanohelices (3 loops, ED = 215 nm, WD = 60 nm, VP = 350 nm, and LP = 400 nm) realized by FEBID. Both arrays are compensated by implementation of a refresh time to facilitate the precursor gas replenishment and to restore the lost pressure in the reservoir for effusion during a time-consuming process.

Therefore, after the investigation of 3D evolution for single loop nanohelix, a detailed analysis was performed on the growth of N-loop structures and periodic array of closely spaced nano-objects by FIBID and FEBID in order to get a significant signal-to-noise ratio in their optical response. For nanohelices grown by focused ion beam, a negative gradient of the vertical pitch, due to 3D proximity effects, was already observed and fully corrected by a properly optimized dose compensation technique.[28]

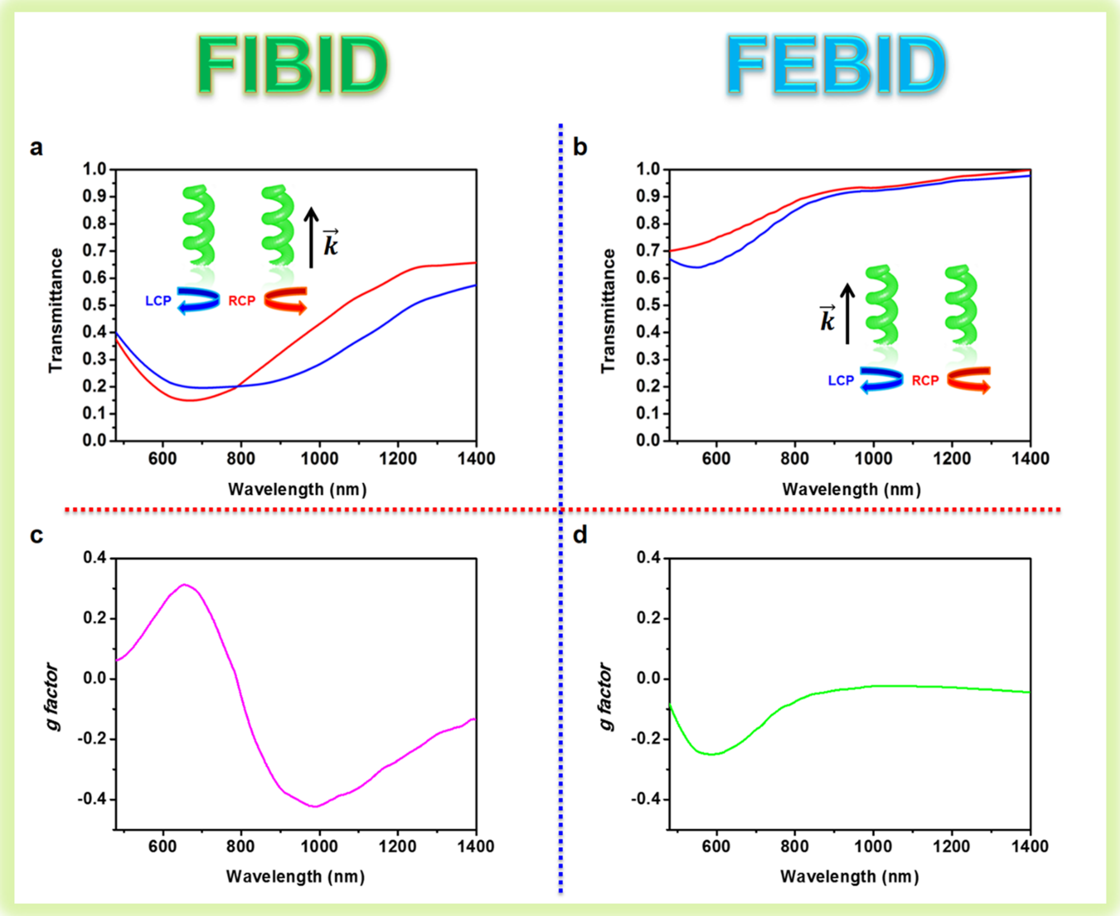

Figure 4. (a) Measured transmission spectra of right- and left- handed circularly polarized light at normal incidence performed on the array shown in Figure 3c. (b) Measured transmission spectra of right- and left-handed circularly polarized light at normal incidence performed on the array shown in Figure 3d. (c, d) Dissymmetry factor g of transmitted spectra for FIBID (Figure 3c) and FEBID (Figure 3d) nanohelix array, respectively.

Similar proximity effects in a single structure are also acting in FEBID process, as an interplay between enhanced multi-scattering processes. During 3D deposition on a pre-existing loop (Figure 2a), according to the ref 44, the PE and the secondary electrons produced by the incident beam (SE^I) are responsible for the vertical growth, while backscattered electrons (BSE) and secondary electrons induced by BSE (SE^{II}) contribute to a radial enlargement of the structure, promoting further nucleation on the lateral surface. Moreover, increasing the acceleration voltage, it is known that PE penetrate better into the deposited material. This results in enhanced multi-scattering processes, where forward scattered electrons (FSE) are generated. FSEs may cross several times the vacuum/grown structure interfaces, generating additional scattering effects, able to finally reach the substrate. This involves a greater amount of deposit and a widening of the nanohelix base and WD.[31,42] For the fabricated nanohelix with two loops, a WD enlargement with respect to the single loop value (from 50 to 70 nm, as shown in Figure 2b) can be observed by increasing the loop number. A proper balance between generation of SE^{II} and penetration in the grown structure was achieved with accelerating voltage of 10 keV along with the dose compensation procedure employed in FIBID[28] (Figure 2c).

For the growth of single nanostructures, 3D proximity effects related only to multiscattered particles must be considered. The situation is different when arrays with a large number of elements should be realized. Figure 3a shows a fabricated linear array of 9 elements by FIBID, spaced by 700 nm, where Pt deposition starts from the left side of the picture and proceeds toward the right side. The figure illustrates the two main effects related to the growth of multiple element arrays and affecting in the same way both the FIBID and FEBID techniques. First of all, we note a slight increase (about 5%) in height from the first nanohelix to the following ones, since the first structure behaves as a mirror for a large portion of precursor gas molecules not ionized by the incident beam,[28,45] thus, increasing the effective molecular flow near the subsequently growing structure. This variation, related to proximity effects, is followed by an additional negative gradient, depending on a slow pressure drop. As a general rule, if the local gas pressure is kept constant during the deposition, all subsequent structures should maintain the same geometric relationships.

The local pressure of gas precursor is strongly interlinked to the writing direction with respect to the gas injection system (GIS)[46] and the area covered by the gas. Optimized flow conditions have been achieved by properly setting the GIS arm lateral and vertical distance, respectively, from the writing zone and from the substrate (see Experimental Section), together with the dose compensation technique[28] to get uniform VP along the nanohelix loops. However, these conditions proved to be effective for small arrays (e.g., 5 × 5 elements in ref 28) where gas pressure drop can be considered negligible, but not for larger

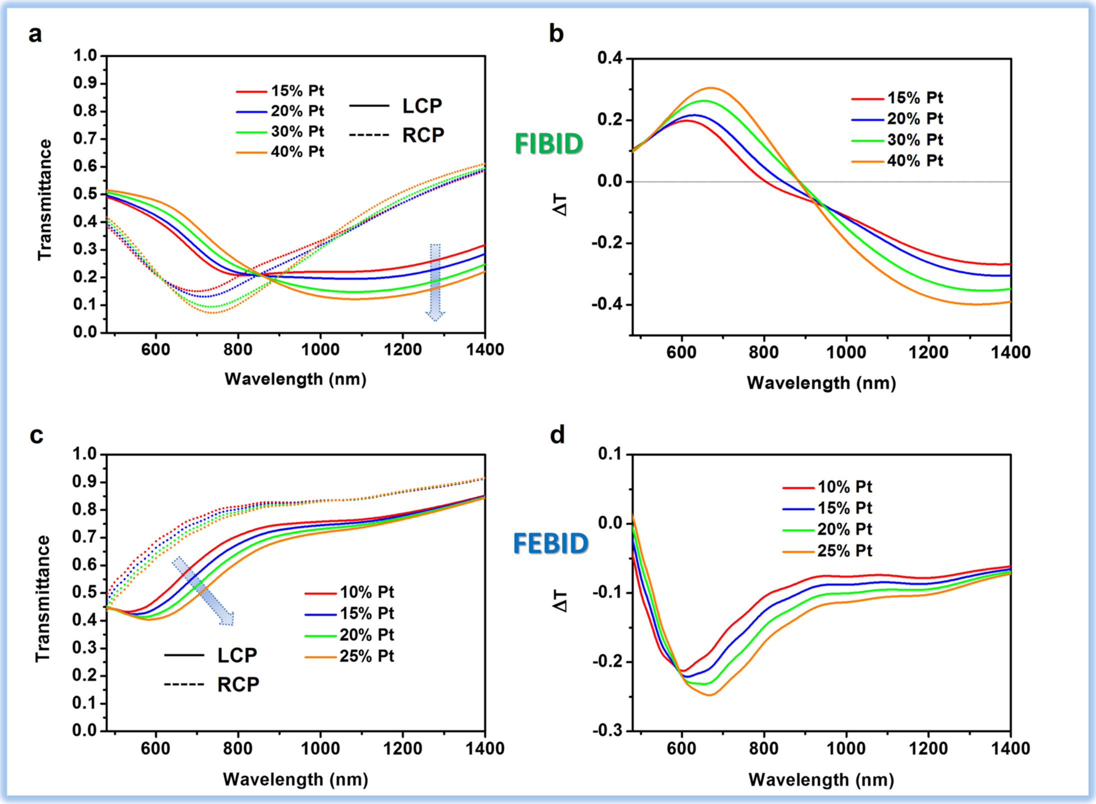

Figure 5. (a) Simulated transmission spectra for the FIBID array shown in Figure 3c of LCP (solid line) and RCP (dashed line) light waves, at normal incidence, as a function of atomic Pt/C concentration. (b) Transmission differences between LCP and RCP light calculated at various Pt percentages. Increasing the Pt content, the resonance and the crossing point red-shifts while the ΔT rises. (c) Simulated transmission spectra for the FEBID array shown in Figure 3d of LCP (solid line) and RCP (dashed line) light as a function of atomic Pt/C concentration. (d) Transmission differences between LCP and RCP light calculated at various Pt percentages. Increasing the Pt content, both resonant wavelength and ΔT increases.

array sizes, where the local pressure reduction becomes significant. Considering the platinum precursor with Knudsen number (Kn) = 1.3[27] and the gas molecules expansion in the main chamber where there is a pressure around 10^{-6} mbar, the mean free path value becomes very large and a molecular flow regime can be expected on the substrate.[27,46] In this condition, precursor population is related to the diffusion, adsorption, and source replenishment. In our case, the gas depletion is enhanced because the multiloop total nanohelix is deposited along the z axis but using the same local area of precursor gas. Therefore, the slow pressure drop due to effusion and the local depletion of the molecular density during the induced deposition process[47−54] can be counterbalanced only with the insertion of a refresh time among the growth of individual nanohelices (Figure 3b, where is showed an array realized by inserting a refresh time of 2 min among the growth of individual nanostructures). This solution resulted effective to provide accurate size control for arrays containing even a very large number of elements[55] as for the array with 20 × 20 nanohelices (3 loops, ED = 400 nm, WD = 130 nm, VP = 300 nm, and Lattice Period LP = 700 nm) shown in Figure 3c, and for the array with 40 × 40 elements (3 loops, ED = 215 nm, WD = 60 nm, VP = 350 nm, and LP = 400 nm) shown in Figure 3d.

The research carried out in order to achieve the full shape evolution control has paved the way toward the ultimate resolution limits in the construction of complex chiral nanohelices by FIBID and FEBID approaches. However, the optimal conditions found (low currents and high acceleration voltages) for the achievement of very high resolutions in the nanostructure fabrication (necessary for applications in the optical region), has a negative counterpart in the chemical composition of the metamaterial, since Pt deposition occurs through the decomposition of the carbon-rich $(CH_3)_3(CH_3C_5H_4)$ Pt precursor, strongly affected by the beam parameters. This results in a reduction of the metallic concentration,[56−58] as will be shown by the analysis of optical transmittance spectra.

Measurement and Theoretical Interpretation of Nanohelix Composition-Dependent Optical Activity. In order to characterize chiral nanohelices array realized by FIBID and FEBID (Figure 3c,d), the transmission spectra under normal incidence of right (T_{RCP})- and left (T_{LCP})-handed circularly polarized light were measured and simulated to evaluate the dissymmetry factor ($g = 2(T_{LCP} - T_{RCP})/(T_{LCP} + T_{RCP})$) through the structures in a range of wavelength between 480 nm and 1.4 μm. Figure 4a shows the measured transmission spectra obtained from a 20 × 20 array of nanohelices by FIBID with edge-to-edge ED of 400 nm, WD of 130 nm, VP of 300 nm, 3 loops and LP of 700 nm (sample shown in Figure 3c). The minimum transmission value for RCP is close to 680 nm, while for LCP there is a quasi-flat minimum zone between 600 and 850 nm, with the crossing point localized approximately at 800 nm. In particular, the dissymmetry factor g reaches its maximum values of 40% at $\lambda \sim 1000$ nm and 30% at $\lambda \sim 650$ nm, as shown in Figure 4c, and a broadband polarization selection of about 600 nm in the near-infrared region.

Figure 4b shows the T_{RCP} and T_{LCP} spectra of the FEBID array (shown in Figure 3d) consisting of 40 × 40 elements, with

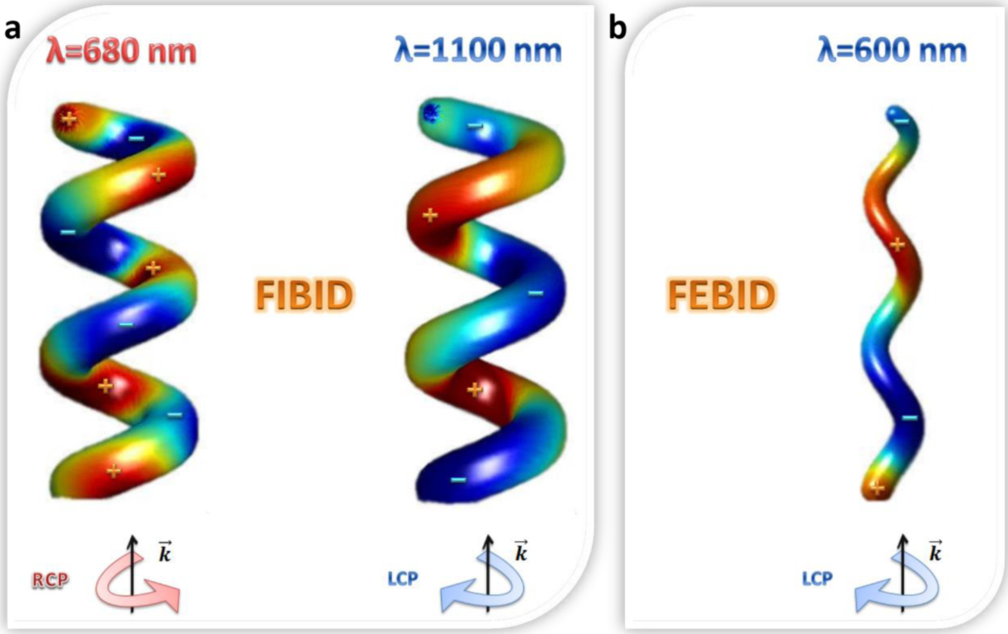

Figure 6. 3D representation of the current oscillation, at (a) λ = 680 and 1100 nm for the FIBID structures, excited by RCP and LCP light, respectively, and (b) λ = 600 nm for the FEBID helix, excited by LCP light.

ED of 215 nm, WD of 60 nm, VP of 350 nm, 3 loops, and LP of 400 nm. The efficient downscaling obtained by exploiting the electron beam, leads to a blue-shift of the optical response with respect to FIBID sample, as theoretically predicted in ref 59 and 60. In fact, the LCP minimum value is blue-shifted down to 600 nm, while the RCP resonance appears much more shifted toward shorter wavelengths. The curves keep nearly the same trend with respect to FIBID array with a higher overall transmission due to the lower density of active material (28% less than in the FIBID case), while the maximum *g* factor of 26% is reached at $\lambda \sim 600$ nm (Figure 4d). Noticeably, with respect to FIBID array, in this case, the circular dichroism operation band extends up to 800 nm and exhibits null dichroism for longer wavelengths,[60] thus, providing a spectrally selective dichroic filtering for circularly polarized visible light in the 480–800 nm band. In both FIBID and FEBID arrays, it is worth noting that, since we are analyzing the optical response in the visible region, very close to the plasmon frequency of the metal structure, the missing light for the low LCP and RCP transmittance is mainly absorbed, as can be inferred by the low reflection spectra (shown in the Supporting Information, Figure S3), with a consequently small contribution of Bragg resonances for the vertical building block arrangement.[24] In addition, increased losses are associated with the large nanohelix effective length.

Measured dichroic properties for different nanohelix dimensions are also reported in the Supporting Information, Figure S4, showing that the entire visible range can be accessed.

Considering that the optical properties of a metamaterial are heavily dependent on its chemical composition and that the actual Pt content of nanostructure strongly depends on the employed beam parameters, we have performed full-wave electromagnetic simulations of the transmission spectra of RCP and LCP light by varying the Pt concentration. For the FIBID structures, a Pt concentration from 15 to 40% (Figure 5a,b) was considered, according to the literature.[57] With increasing Pt amount, the T_{LCP} signal undergoes an enhanced absorption in the near-infrared region, where a large valley centered at 1100 nm arises, whose depth increases with the platinum concentration. On the other hand, in the visible region of the spectrum, the T_{LCP} slightly increases. Conversely, the reduction of the carbon percentage in the alloy implies a substantial increase of the T_{RCP} resonance depth in the visible range together with a redshift of the minimum value. These variations jointly lead to a gradual increase of the optical activity (OA), as expressed by the transmittance difference among the two polarizations (ΔT) with the Pt concentration over the whole observed spectral region (Figure 5b). The simulations also show that a higher metal concentration in the carbon matrix further enhances the redshift of the crossing point. A good agreement has been observed between experimental transmission and simulated curves with a Pt content between 15 and 20%, consistent with the used beam parameters.[57]

In the FEBID sample (Figure 5c,d), where a Pt concentration from 10 to 25% was considered, both, LCP and RCP transmission decrease with increasing Pt content, with a red shift of the T_{LCP} minimum comparable to the one observed in the visible region for the FIBID sample. Accordingly, ΔT increases with the metal content (Figure 5d). A good agreement between experimental transmission and simulated curves has been observed with a Pt content of 10%.

Together with the effect of Pt content on OA, fabrication tolerances, and their effect on transmission spectra were also considered by simulations. SEM inspection of the fabricated arrays determined a tolerance range of 10% for VP and ED, which was considered in calculated transmission spectra shown in the Supporting Information, Figure S6. This analysis shows the critical role played by the ED in shifting the transmission spectra, in good agreement with previously reported studies.[59,60] On the other hand, variations of the VP value within the tolerance range induce a negligible shift of the curves. As far as WD changes are concerned, the estimated tolerance is less than 5% and, apart from the most relevant geometrical effect on ED, it is expected to slightly affect the amount of transmitted light.

These considerations allow us to use the measured mean values of geometrical dimensions as input for the numerical simulations.

To clarify the resonance positions, we can also use the plasmon hybridization model.[61] In particular, our three-loop helix can be considered as a periodic arrangement, along the third dimension, of a unit cell,[62] similar to the structure discussed in ref 63. The mutual proximity of each unit cell leads to boosted resonance hybridization of single cell resonance modes, yielding the broad stop-band observed for both circular polarizations in the FIBID and FEBID transmission spectra. In Figure 6 we theoretically analyze the electromagnetic interaction between circularly polarized light and the helical structure in terms of plasmon oscillations (electric dipoles in Figure 6, where the different direction is highlighted by red and blue colors). In particular, we simulated the current oscillations, excited by circularly polarized light, at each resonance position found from transmittance spectra for FIBID and FEBID structures, respectively. On the basis of the dipole model,[63] the dipole arrangement depends on the mutual orientation of the circularly polarized light and the nanohelix handedness, according to the frequency under investigation and to the dimensional parameters. Considering the right-handed FIBID structures, RCP light is strongly absorbed at λ = 680 nm due to a good matching between RCP light and helix twist. On the other hand, the LCP light exhibits, at the center frequency of the quasi-flat band (1100 nm), a local transmittance minimum, since the LCP light fits well with the arrangement of the dipoles in the structure at this wavelength. Moreover, analyzing the simulated current oscillations for FIBID structure in Figure 6a, we note that the current oscillation at the RCP resonance (λ = 680 nm) exhibits more nodes than at the LCP resonance (λ = 1100 nm), resulting in a higher energy configuration with respect to the LCP resonance.[63] A similar discussion can be carried out for FEBID structures, where the nanoscaling of the geometric dimensions has led to a large blue-shift of the transmission spectra. Here, a hybridized stop band is present for LCP transmission spectrum with a minimum value at λ = 600 nm, with a low number of current oscillation nodes (Figure 6b), while the RCP stop band seems shifted toward higher frequencies out of the investigated spectral range.

CONCLUSION

We have shown the nanoscaling by FIBID and FEBID techniques of chiral plasmonic structures in the form of 3D platinum nanohelices with circular dichroism band in the optical regime, tailored by nanostructure sizes. The study of the shape evolution as a function of involved technological parameters enabled us to accurately control the geometrical features of the proposed 3D nanostructures in a wide dimensional range, thus, allowing a large control of their spectral operating region with structure sizes.

Nanohelices with external diameter between 500 and 150 nm, WD from 130 down to 50 nm, and VP down to 200 nm have been successfully controlled. Transmission measurements for circularly polarized light show a maximum dissymmetry factor up to 40% at $\lambda \sim 1000$ nm for helix array of larger sizes realized by FIBID and up to 26% at $\lambda \sim 600$ nm for the helix array with reduced sizes fabricated by FEBID. Moreover, a high selectivity of the dichroic band is evidenced, accompanied by the shift of operational range toward the visible. In addition, a detailed FDTD model was developed to explain the interaction of circularly polarized light with fabricated 3D metallic nanohelices at different frequencies, highlighting the role played by geometrical as well as compositional parameters. Further developments of this study may include the strong enhancement of the optical activity by the increment of platinum content. The presented nanostructures find a natural application in nanophotonics devices either as integrated nanoscale broadband and/or wavelength selective circular polarizers in the entire visible range or for the biological detection based on circular dichroism spectroscopy.

EXPERIMENTAL SECTION

Sample Preparation. GaN/AlGaN heterostructures grown on sapphire substrates were employed for the nanostructure growth.[28,67] Substrates were cleaned with acetone and isopropanol and loaded in a dual configuration Focused Ion Beam/Scanning Electron Microscopy (FIB/SEM) system, the Carl Zeiss Auriga40 Crossbeam, equipped with the Cobra FIB column and a gas injection system (GIS) with five gas channels. For both FIBID and FEBID nanohelices, we employed trimethyl(methylcyclopentadienyl)-platinum(IV) precursor, locally injected through the nozzle at the upper side of the sample. The inner and outer needle diameters are 300 and 500 μm, respectively. The gas pressure was stabilized for 5 min at the precursor temperature of 80 °C to reduce variations in the growth rate. The nanohelices were made through a scanning direction orthogonal to the precursor gas flow, and the gas injection system main axis is aligned with respect to the upper side of the deposition area. The vertical and lateral injection distance from the nozzle to the substrate surface and the nucleation area were optimized in order to get a gas local density suitable for controlled 3D growth. For FIBID (FEBID), the optimized flow conditions have been achieved with the GIS arm at 100 μm (260 μm) away, in the lateral direction, from the writing zone, 100 μm (100 μm) in height from the substrate, and with the needle tilt angle of 70° (16°) with respect to the substrate. Before growth, the chamber pressure was 1×10^{-6} mbar while, during the whole deposition process, the chamber pressure ranged from 1×10^{-5} mbar to 8×10^{-6} mbar. SEM images of the growing structures were taken in the coincidence point of the ion and electron beam, after adjusting the tilt eccentricity, to measure loop diameters, vertical pitch, and horizontal period, taking into account the proper stage tilt. The Raith Elphy Multibeam pattern generator controlled exposure parameters of both beams. The base pattern layout consists of an empty circle that is scanned several times by the ion or electron beam.

Optical Transmittance Spectroscopy. Transmission spectra on nanohelices array have been performed in a confocal configuration by using a 10× objective lens with numerical aperture (NA) = 0.45[28] under normal incidence illumination of a tungsten lamp. RCP and LCP light have been generated using a linear polarizer coupled with an achromatic quarter waveplate. Light was focused on the sample by means of a condenser lens with NA = 0.3. All measurements have been taken with the microscope iris diaphragm as close as possible (5 mm diameter pinhole) to illuminate a circular area having a 200 μm diameter with a light cone of approximately 18° semiaperture angle. At the exit of the microscope, a slit has been placed in the focal plane, in order to select the signal coming from the nanohelices array. The selected real image is reconstructed and directed to a CCD camera (Hamamatsu Orca R2) coupled with a 200 mm spectrometer for measurements in the visible spectral range or to an InGaAs detector coupled with a 300 mm spectrometer for measurements in the near-infrared region of the spectrum. All transmission measurements were normalized to the optical response of the substrate.

Simulations. To evaluate the spectral properties of the FIBID-class helix samples, we simulated the electromagnetic response in the visible and infrared range of a periodic arrangement of helices virtually composed of a carbon—platinum alloy. The material permittivity (discussed and shown in Supporting Information, Figure S5) has been evaluated retrieving the measured values of the two distinct components (Pt and C) in literature[64] and then by mixing them with the Maxwell-Garnett approach.[65,66] All the simulations have been performed in Lumerical FDTD Solutions, and the postprocessing of data have been completed by means of several Matlab codes. The helix type have been performed varying linearly the WR starting from 65 nm for the bottom layers to 55 nm to the top layers, with a VP of 300 nm, a skeleton radius (SR) of 105 nm, loop number of 3 and the helices mutual distance in the periodic square grid of 700 nm. To reduce any spurious scattering at sharp borders, we smoothened the terminal tips at both sides of the helix by making them round. The substrate has not been included in the simulations.

■ ASSOCIATED CONTENT

Ⓢ Supporting Information

Detailed dependences of the geometrical features on the pattern parameters used for efficient nanoscaling of the nanostructures, along with the measured reflectance spectra of the FIBID array, the dispersion law employed for the theoretical simulations, and the g factor of different size arrays are available. This material is available free of charge via the Internet at http://pubs.acs.org.

■ AUTHOR INFORMATION

Corresponding Author

*E-mail: marco.esposito@nano.cnr.it.

Notes

The authors declare no competing financial interest.

■ ACKNOWLEDGMENTS

The work was partially supported by the National Project PON “Beyond Nano” “R&C” 2007-2013 PONa3_00362, by the MARINE project, and by the ERC POLAFLOW Grant Number 308136.

■ REFERENCES

(1) Pendry, J. B. Negative Refraction Makes a Perfect Lens. *Phys. Rev. Lett.* **2000**, *85*, 3966−3969.

(2) Pendry, J. B.; Schurig, D.; Smith, D. R. Controlling Electromagnetic Fields. *Science* **2006**, *312*, 1780−1782.

(3) Hess, O.; Pendry, J. B.; Maier, S. A.; Oulton, R. P.; Hamm, J. M.; Tsakmakidis, K. L. Active Nanoplasmonic Metamaterials. *Nat. Mater.* **2012**, *11*, 573−584.

(4) Soukoulis, C. M.; Wegener, M. Past Achievements and Future Challenges in the Development of Three-Dimensional Photonic Metamaterials. *Nat. Photonics* **2011**, *5*, 523−530.

(5) Luk'yanchuk, B.; Zheludev, N. I.; Maier, S. A.; Halas, N. J.; Nordlander, P.; Giessen, H.; Chong, C. T. The Fano Resonance in Plasmonic Nanostructures and Metamaterials. *Nat. Mater.* **2010**, *9*, 707−715.

(6) Smith, D. R.; Pendry, J. B.; Wiltshire, M. C. K. Metamaterials and Negative Refractive Index. *Science* **2004**, *305*, 788−792.

(7) Pendry, J. B. A Chiral Route to Negative Refraction. *Science* **2004**, *306*, 1353−1355.

(8) Wiltshire, M. C. K.; Pendry, J. B.; Hajnal, J. V. Chiral Swiss Rolls Show a Negative Refractive Index. *J. Phys.: Condens. Matter.* **2009**, *21*, 292201.

(9) Valev, V. K.; Baumberg, J. J.; Sibilia, C.; Verbiest, T. Chirality and Chiroptical Effects in Plasmonic Nanostructures: Fundamentals, Recent Progress, and Outlook. *Adv. Mater.* **2013**, *25*, 2517−2534.

(10) Plum, E.; Zhou, J.; Dong, J.; Fedotov, V.; Koschny, T.; Soukoulis, C. M.; Zheludev, N. I. Metamaterial with Negative Index Due to Chirality. *Phys. Rev. B* **2009**, *79*, 035407.

(11) Decker, M.; Zhao, R.; Soukoulis, C. M.; Linden, S.; Wegener, M. Twisted Split-Ring-Resonator Photonic Metamaterial with Huge Optical Activity. *Opt. Lett.* **2010**, *35*, 1593−1595.

(12) Shadrivov, I. V.; Fedotov, V. A.; Powell, D. A.; Kivshar, Y. S.; Zheludev, N. I. Electromagnetic Wave Analogue of an Electronic Diode. *New J. Phys.* **2011**, *13*, 033025.

(13) Wang, B.; Zhou, J.; Koschny, T.; Kafesaki, M.; Soukoulis, C. M. Chiral Metamaterials: Simulations and Experiments. *J. Opt. A: Pure Appl. Opt.* **2009**, *11*, 114003.

(14) Rockstuhl, C.; Menzel, C.; Paul, T.; Lederer, F. Optical Activity in Chiral Media Composed of Three-Dimensional Metallic Meta-Atoms. *Phys. Rev. B* **2009**, *79*, 035321.

(15) Kuwata-Gonokami, M.; Saito, N.; Ino, Y.; Kauranen, M.; Jefimovs, K.; Vallius, T.; Turunen, J.; Svirko, Y. Giant Optical Activity in Quasi-Two-Dimensional Planar Nanostructures. *Phys. Rev. Lett.* **2005**, *95*, 227401.

(16) Eftekhari, F.; Davis, T. Strong Chiral Optical Response from Planar Arrays of Subwavelength Metallic Structures Supporting Surface Plasmon Resonances. *Phys. Rev. B* **2012**, *86*, 075428.

(17) Yin, X.; Schäferling, M.; Metzger, B.; Giessen, H. Interpreting Chiral Nanophotonic Spectra: The Plasmonic Born−Kuhn Model. *Nano Lett.* **2013**, *13*, 6238−6243.

(18) Plum, E.; Fedotov, V. A.; Schwanecke, A. S.; Zheludev, N. I.; Chen, Y. Giant Optical Gyrotropy due to Electromagnetic Coupling. *Appl. Phys. Lett.* **2007**, *90*, 223113.

(19) Liu, N.; Liu, H.; Zhu, S. N.; Giessen, H. Stereometamaterials. *Nat. Photonics* **2009**, *3*, 157−162.

(20) Helgert, C.; Pshenay-Severin, E.; Falkner, M.; Menzel, C.; Rockstuhl, C.; Kley, E.-B.; Tünnermann, A.; Lederer, F.; Pertsch, T. Chiral Metamaterial Composed of Three-Dimensional Plasmonic Nanostructures. *Nano Lett.* **2011**, *11*, 4400−4404.

(21) Christofi, A.; Stefanou, N.; Gantzounis, G.; Papanikolaou, N. Giant Optical Activity of Helical Architectures of Plasmonic Nanorods. *J. Phys. Chem. C* **2012**, *116*, 16674−16679.

(22) Decker, M.; Ruther, M.; Kriegler, C. E.; Zhou, J.; Soukoulis, C. M.; Linden, S.; Wegener, M. Strong Optical Activity from Twisted-Cross Photonic Metamaterials. *Opt. Lett.* **2009**, *34*, 2501−2503.

(23) Zhao, Y.; Belkin, M. A.; Alù, A. Twisted Optical Metamaterials for Planarized Ultrathin Broadband Circular Polarizers. *Nat. Commun.* **2012**, *3*, 870.

(24) Gansel, J. K.; Thiel, M.; Rill, M. S.; Decker, M.; Bade, K.; Saile, V.; von Freymann, G.; Linden, S.; Wegener, M. Gold Helix Photonic Metamaterial as Broadband Circular Polarizer. *Science* **2009**, *325*, 1513−1515.

(25) Gansel, J. K.; Latzel, M.; Frolich, A.; Kaschke, J.; Thiel, M.; Wegener, M. Tapered Gold-Helix Metamaterials as Improved Circular Polarizers. *Appl. Phys. Lett.* **2012**, *100*, 101109.

(26) Matsui, S.; Kaito, T.; Fujita, J.; Komuro, M.; Kanda, K.; Haruyama, Y. Three-Dimensional Nanostructure Fabrication by Focused-Ion-Beam Chemical Vapor Deposition. *J. Vac. Sci. Technol., B* **2000**, *18*, 3181−3184.

(27) Utke, I.; Hoffmann, P.; Melngailis, J. Gas-Assisted Focused Electron Beam and Ion Beam Processing and Fabrication. *J. Vac. Sci. Technol., B* **2008**, *26*, 1197−1276.

(28) Esposito, M.; Tasco, V.; Todisco, F.; Benedetti, A.; Sanvitto, D.; Passaseo, A. Three Dimensional Chiral Metamaterial Nanospirals in the Visible Range by Vertically Compensated Focused Ion Beam Induced-Deposition. *Adv. Opt. Mater.* **2013**, *2*, 154−161.

(29) Koops, H.; Kretz, J.; Rudolph, M.; Weber, M. Constructive Three-Dimensional Lithography with Electron-Beam Induced Depo-

sition for Quantum Effect Devices. *J. Vac. Sci. Technol., B* **1993**, *11*, 2386−2389.

(30) Lipp, S.; Frey, L.; Lehrer, C.; Demm, E.; Pauthner, S.; Ryssel, H. A Comparison of Focused Ion Beam and Electron Beam Induced Deposition Processes. *Microelectron. Reliab.* **1996**, *36*, 1779−1782.

(31) van Dorp, W. F.; Hagen, C. W. A Critical Literature Review of Focused Electron Beam Induced Deposition. *J. Appl. Phys.* **2008**, *104*, 081301.

(32) Boggild, P.; Hansen, T. M.; Tanasa, C.; Grey, F. Fabrication and Actuation of Customized Nanotweezers with a 25 nm Gap. *Nanotechnology* **2001**, *12*, 331−335.

(33) Chen, P.; Salemink, H. W. M.; Alkemade, P. F. A. Roles of Secondary Electrons and Sputtered Atoms in Ion-Beam-Induced Deposition. *J. Vac. Sci. Technol., B* **2009**, *27*, 2718−2721.

(34) Dubner, A. D.; Wagner, A.; Melngailis, J.; Thompson, C. V. The Role of the Ion-Solid Interaction in Ion-Beam-Induced Deposition of Gold. *J. Appl. Phys.* **1991**, *70*, 665−673.

(35) Ro, J. S.; Thompson, C. V.; Melngailis, J. Mechanism of Ion-Beam-Induced Deposition of Gold. *J. Vac. Sci. Technol., B* **1994**, *12*, 73−77.

(36) Hoyle, P.; Cleaver, J.; Ahmed, H. Ultralow-Energy Focused Electron Beam Induced Deposition. *Appl. Phys. Lett.* **1994**, *64*, 1448−1450.

(37) Takai, M.; Jarupoonphol, W.; Ochiai, C.; Yavas, O.; Park, Y. K. Processing of Vacuum Microelectronic Devices by Focused Ion and Electron Beams. *Appl. Phys. A: Mater. Sci. Process* **2003**, *76*, 1007−1012.

(38) Bauerdick, S.; Burkhardt, C.; Rudorf, R.; Barth, W.; Bucher, V.; Nisch, W. In Situ Monitoring of Electron Beam Induced Deposition by Atomic Force Microscopy in a Scanning Electron Microscope. *Microelectron. Eng.* **2003**, *67−68*, 963−969.

(39) Beaulieu, D.; Ding, Y.; Wang, Z. L.; Lackey, W. J. Influence of Process Variables on Electron Beam Chemical Vapor Deposition of Platinum. *J. Vac. Sci. Technol., B* **2005**, *23*, 2151−2159.

(40) Ding, W.; Dikin, D. A.; Chen, X.; Piner, R. D.; Ruoff, R. S.; Zussman, E.; Wang, X.; Li, X. Mechanics of Hydrogenated Amorphous Carbon Deposits from Electron Beam Induced Deposition of a Paraffin Precursor. *J. Appl. Phys.* **2005**, *98*, 014905.

(41) Croitoru, M. D.; Bertsche, G.; Kern, D. R.; Burkhardt, C.; Bauerdick, S.; Şahakalkan, S.; Roth, S. Visualization and In Situ Contacting of Carbon Nanotubes in a Scanning Electron Microscope. *J. Vac. Sci. Technol., B* **2005**, *23*, 2789−2792.

(42) Bret, T.; Utke, I.; Gaillard, C.; Hoffmann, P. Periodic Structure Formation by Focused E-Beam Deposition. *J. Vac. Sci. Technol., B* **2004**, *22*, 2504−2510.

(43) Li, Y. R.; Ho, R. M.; Hung, Y. C. Plasmon Hybridization and Dipolar Interaction on the Resonances of Helix Metamaterials. *IEEE Photonics J.* **2013**, *5*, 2700510.

(44) Fowlkes, J. D.; Randolph, S. J.; Rack, P. D. Growth and Simulation of High-Aspect Ratio Nanopillars by Primary and Secondary Electron-Induced Deposition. *J. Vac. Sci. Technol., B* **2005**, *23*, 2825−2832.

(45) Chen, P.; Salemink, H. W. M.; Alkemade, P. F. A. Proximity Effect in Ion-Beam-Induced Deposition of Nanopillars. *J. Vac. Sci. Technol., B* **2009**, *27*, 1838−1843.

(46) Bret, T.; Utke, I.; Hoffmann, P. Influence of the Beam Scan Direction during Focused Electron Beam Induced Deposition of 3D Nanostructures. *Microelectron. Eng.* **2005**, *78*, 307−313.

(47) Chiang, T. P.; Sawin, H. H.; Thompson, C. V. Surface Kinetic Study of Ion-Induced Chemical Vapor Deposition of Copper for Focused Ion beam Applications. *J. Vac. Sci. Technol., A* **1997**, *15*, 3104−3114.

(48) Smith, D. A.; Fowlkes, J. D.; Rack, P. D. Simulating the Effects of Surface Diffusion on Electron Beam Induced Deposition via a Three-Dimensional Monte Carlo Simulation. *Nanotechnology* **2008**, *19*, 415704−415714.

(49) Smith, D. A.; Fowlkes, J. D.; Rack, P. D. Understanding the Kinetics and Nanoscale Morphology of Electron-Beam-Induced Deposition via a Three-Dimensional Monte Carlo Simulation: The Effects of the Precursor Molecule and the Deposited Material. *Small* **2008**, *4*, 1382−1389.

(50) Fowlkes, J. D.; Doktycz, M. J.; Rack, P. D. An Optimized Nanoparticle Separator Enabled by Electron Beam Induced Deposition. *Nanotechnology* **2010**, *21*, 165303−165311.

(51) Plank, H.; Gspan, C.; Dienstleder, M.; Kothleitner, G.; Hofer, F. The Influence of Beam Defocus on Volume Growth Rates for Electron Beam Induced Platinum Deposition. *Nanotechnology* **2008**, *19*, 485302−485311.

(52) Plank, H.; Smith, D. A.; Haber, T.; Rack, P. D.; Hofer, F. Fundamental Proximity Effects in Focused Electron Beam Induced Deposition. *ACS Nano* **2012**, *6*, 286−294.

(53) Choi, Y. R.; Rack, P. D.; Randolph, S. J.; Smith, D. A.; Joy, D. C. Pressure Effect of Growing with Electron Beam-Induced Deposition with Tungsten Hexafluoride and Tetraethylorthosilicate Precursor. *Scanning* **2006**, *28*, 311−318.

(54) Tanaka, M.; Shimojo, M.; Mitsuishi, K.; Furuya, K. The Size Dependence of the Nano-Dots Formed by Electron-Beam-Induced Deposition on the Partial Pressure of the Precursor. *Appl. Phys. A: Mater. Sci. Process.* **2004**, *78*, 543−546.

(55) Fowlkes, J. D.; Rack, P. D. Fundamental Electron-Precursor-Solid Interactions Derived from Time-Dependent Electron-Beam-Induced Deposition Simulations and Experiments. *ACS Nano* **2010**, *4*, 1619−1629.

(56) De Teresa, J. M.; Córdoba, R.; Fernández-Pacheco, A.; Montero, O.; Strichovanec, P.; Ibarra, M. R. Origin of the Difference in the Resistivity of As-Grown Focused-Ion- and Focused-Electron-Beam-Induced Pt Nanodeposits. *J. Nanomater.* **2009**, *2009*, 936863.

(57) Wiedemair, J.; Menegazzo, N.; Pikarskyc, J.; Booksh, K. S.; Mizaikoff, B.; Kranz, C. Novel Electrode Materials Based on Ion Beam Induced Deposition of Platinum Carbon Composites. *Electrochim. Acta* **2010**, *55*, 5725−5732.

(58) Koops, H. W. P.; Kaya, A.; Weber, M. Fabrication and Characterization of Platinum Nanocrystalline Material Grown by Electron Beam Induced Deposition. *J. Vac. Sci. Technol., B* **1995**, *13*, 2400−2403.

(59) Gansel, J. K.; Wegener, M.; Burger, S.; Linden, S. Gold Helix Photonic Metamaterials: A Numerical Parameter Study. *Opt. Express* **2010**, *18*, 1059−1069.

(60) Yang, Z. Y.; Zhao, M.; Lu, P. X. A Numerical Study on Helix Nanowire Metamaterials as Optical Circular Polarizers in the Visible Region. *IEEE Photonics Technol. Lett.* **2010**, *22*, 1303−1305.

(61) Prodan, E.; Radloff, C.; Halas, N. J.; Nordlander, P. A Hybridization Model for the Plasmon Response of Complex Nanostructures. *Science* **2003**, *302*, 419−422.

(62) Plum, E.; Liu, X.-X.; Fedotov, V. A.; Chen, Y.; Tsai, D. P.; Zheludev, N. I. Metamaterials: Optical Activity without Chirality. *Phys. Rev. Lett.* **2009**, *102*, 113902.

(63) Frank, B.; Yin, X.; Schäferling, M.; Zhao, J.; Hein, S. M.; Braun, P. V.; Giessen, H. Large-Area 3D Chiral Plasmonic Structures. *ACS Nano* **2013**, *7*, 6321−6329.

(64) Palik, E. D. *Handbook of Optical Constants of Solids*; Academic Press: New York, 1991.

(65) Maxwell, G. J. C. Colours in Metal Glasses and Metal Films. *Philos. Trans. R. Soc. London, Sect. A* **1904**, *3*, 385−420.

(66) Wenshan, C.; Shalaev, V. *Optical Metamaterials: Fundamentals and Applications*; Springer: New York, 2009.

(67) Tasco, V.; Campa, A.; Tarantini, I.; Passaseo, A.; González-Posada, F.; Redondo-Cubero, A.; Lorenz, K.; Franco, N.; Muñoz, E. Investigation of Different Mechanisms of GaN Growth Induced on AlN and GaN Nucleation Layers. *J. Appl. Phys.* **2009**, *105*, 063510.